

## POROSITY AND BAND-STRENGTH MEASUREMENTS OF MULTI-PHASE COMPOSITE ICES

JEAN-BAPTISTE BOSSA<sup>1</sup>, BELÉN MATÉ<sup>2</sup>, COEN FRANSEN<sup>1</sup>, STÉPHANIE CAZAUX<sup>1,3</sup>, SERGIO PILLING<sup>4</sup>,  
WILL ROBSON MONTEIRO ROCHA<sup>4</sup>, JUAN ORTIGOSO<sup>2</sup>, AND HAROLD LINNARTZ<sup>1</sup><sup>1</sup> Sackler Laboratory for Astrophysics, Leiden Observatory, Leiden University, P.O. Box 9513, NL-2300 RA Leiden, The Netherlands<sup>2</sup> Instituto de Estructura de la Materia, IEM-CSIC, Serrano 123, E-28006 Madrid, Spain<sup>3</sup> Kapteyn Astronomical Institute, P.O. Box 800, 9700 AV Groningen, The Netherlands<sup>4</sup> Instituto de Pesquisa & Desenvolvimento, Universidade do Vale do Paraíba, São José dos Campos, SP 12244000, Brazil

Received 2015 September 4; accepted 2015 October 8; published 2015 November 17

## ABSTRACT

We use experimental mid-infrared optical constants and extended effective medium approximations to determine the porosity and the band strengths of multi-phase composite ices grown at 30 K. A set of porous H<sub>2</sub>O:CH<sub>4</sub> ices are taken as a prototypical example. As a benchmark and proof of concept, the stoichiometry of the ice constituents is retrieved with good accuracy from the refractive indices and the extinction coefficients of the reference binary ice mixtures with known compositions. Accurate band strengths are then calculated from experimental mid-infrared spectra of complex ices. We notice that the presence of pores has only a small effect on the overall band strengths, whereas a water dilution can considerably alter them. Different levels of porosity are observed depending on the abundance of methane used as a gas contaminant premixed with water prior to background deposition. The absorption profiles are also found to vary with deposition rate. To explain this, we use Monte Carlo simulations and we observe that the deposition rate strongly affects the pore size distribution as well as the ice morphology through reorganization processes. Extrapolated to genuine interstellar ices, the methodology presented in this paper can be used to evaluate the porosity and to quantify the relative abundances from observational data.

*Key words:* ISM: molecules – methods: laboratory: solid state

## 1. INTRODUCTION

Amorphous solid water is the predominant form of water observed in dense molecular clouds and around young stellar objects (Gibb et al. 2004; Boogert et al. 2008, 2015; van Dishoeck et al. 2013), in comets, and in icy satellite surfaces of the outer solar system (Dalton et al. 2010). It has been experimentally demonstrated that compact (i.e., non-porous) amorphous solid water is mainly formed at low temperature through grain-surface reactions involving precursors such as O, O<sub>2</sub>, O<sub>3</sub>, H, H<sub>2</sub>, and OH (Ioppolo et al. 2008, 2010; Miyauchi et al. 2008; Dulieu et al. 2009; Oba et al. 2009; Cuppen et al. 2010; Romanzin et al. 2010; Linnartz et al. 2015). In parallel, other laboratory data have proven that direct vapour deposition of water on a cold substrate results in a two-phase composite ice by taking the presence of pores into account, which are inevitably formed during growth (Stevenson et al. 1999). The resulting degree of porosity depends on experimental conditions, such as the growth temperature, the deposition rate, the growth angle (Brown et al. 1996; Dohnálek et al. 2003; Maté et al. 2012), and in the specific case of a gas mixture, the nature and the abundance of the premixed constituents (Bossa et al. 2014). Whereas many observational studies have focused on the chemical composition of interstellar ices, much less effort has been put into determining the actual level of porosity. A variety of factors can influence the level of porosity. Energetic processes can drastically reduce the number of pores (Palumbo 2006; Raut et al. 2007, 2008; Palumbo et al. 2010; Accolla et al. 2011), while omnidirectional deposition after non-thermal desorption (Greenberg 1973; McKee 1989; Bergin et al. 1999; Cazaux et al. 2010; Fayolle et al. 2011; Williams & Cieza 2011; Dulieu et al. 2013) can enhance porosity. Given the diversity of environments where ices have been observed, one can expect a wide porosity range in space. Quantifying the porosity of

interstellar ices from observational data is key to understanding the molecular complexity seen toward low- and high-mass protostars; the level of porosity determines the efficiency of the adsorption, the diffusion, the reaction, and the entrapment capacities of astrophysically relevant molecules. By providing large effective surface areas, pores have important consequences for the chemistry governed by surface processes. So far, remote observations of interstellar ices have converged to the same conclusion that porosity is rare in space (Keane et al. 2001). The missing O–H dangling features near 3700 cm<sup>-1</sup> (2.7 μm) in both astronomical and laboratory spectra have been taken as proof of compact amorphous solid water in the ISM. However, care should be taken, since laboratory data and simulations demonstrate that the absence of the O–H dangling modes does not necessarily imply the complete absence of porosity (Raut et al. 2007; Isokoski et al. 2014; Cazaux et al. 2015). An alternative probing tool is therefore mandatory to quantify the level of ice porosity in space.

Remote observations of star-forming regions performed by space telescopes have provided the inventory of interstellar ice components (Gibb et al. 2004; Boogert et al. 2008; Öberg et al. 2008) and the abundances of these species are deduced from accurate optical constants ( $N = n - ik$ ) with reference spectra obtained in mid-infrared laboratory studies, generally based on pure ice constituents. Starting from this principle, our main goal is to characterize how the number of pores and the abundance of a contaminant (e.g., CH<sub>4</sub>) affect the mid-infrared optical constants of a porous composite ice dominated by water. That is, we extend existing work to mixed ices including porosity effects. Depending on the amplitude of the alteration, this investigation holds the potential to determine the porosity and the band strengths of multi-phase composite ices. As one might expect, the first

difficulty to face is the countless possible combinations involving pores, water, and methane. Since it is impossible to determine experimentally the whole set of optical constants, the use of a theoretical treatment is required for each case. Based on effective medium approximations (EMAs), namely those of Maxwell Garnett (1904, 1906) and Bruggeman (1935), we first calculate the effective mid-infrared optical constants of a large set of fictive porous  $\text{H}_2\text{O}:\text{CH}_4$  ices. Then, we compare the whole effective data set with experimental values obtained from the mid-infrared spectra of ices grown in the laboratory with known thicknesses and relative abundances. From the mid-infrared spectra, we can extract the wavelength-dependent experimental optical constants using a Kramers–Kronig analysis. EMAs have already proven to provide fairly good predictions of optical constants in the mid-infrared range for binary ice mixtures (Mukai & Mukai 1984; Mukai & Krättschmer 1986; Mukai et al. 1987). Here for the first time, these well known EMAs are used in their extended forms (Niklasson et al. 1981; Luo 1997) to characterize the porosity of multi-phase composite ices using mid-infrared data. Such results offer a much needed tool to model spectra, determine accurate band strengths, and estimate abundances of pores and ice constituents in interstellar clouds (preferably unprocessed ices). The results allow existing infrared observations from the *Infrared Space Observatory* and *Spitzer Space Telescope* to be interpreted and will be valuable in guiding future observations with the *James Webb Space Telescope*.

This study focuses on amorphous solid water ice containing methane ( $\text{CH}_4$ ). Interstellar methane likely forms on the surface of cold grains through successive hydrogenations of carbon atoms, in a process similar to that observed for the formation of methanol ( $\text{CH}_3\text{OH}$ ) from carbon monoxide ( $\text{CO}$ ) (Watanabe et al. 2004; Fuchs et al. 2009). In addition, first-order photodissociation reactions of more complex precursors leading to  $\text{CH}_4$  cannot be neglected (Bossa et al. 2015). Depending on the line of sight, typical  $\text{CH}_4$  concentrations range between 0.5% and 5% relative to water; however, an upper limit of 13% has been determined in a few cases (Öberg et al. 2008). Methane has also been identified in outer solar system objects (Licandro et al. 2006) and in comets (Gibb et al. 2003). The relevance of the  $\text{H}_2\text{O}:\text{CH}_4$  system is emphasized by the numerous studies dedicated to the different physical and chemical interactions between these two species, including clathrates (Dartois & Deboffle 2008), aerosols, and ice mixtures (Gálvez et al. 2009; Pilling et al. 2009; Herrero et al. 2010). Finally, methane molecules embedded in a porous water matrix offer an excellent test system because trapping effects are largely dominant (Ayotte et al. 2001; Collings et al. 2003) and one of the main prerequisites for accurate estimations of optical constants is to keep interactions between components as small as possible (Mukai et al. 1987). The present study combines experimental and theoretical results and focuses on composite ices made of water, methane, and pores. The paper is organized in the following way. Section 2 describes details of the experimental and theoretical methods, fitting procedure, and data interpretation. Results are presented in Section 3. The astronomical relevance of this work is discussed in Section 4. A summary and concluding remarks are given in the final section.

## 2. LABORATORY PROCEDURES AND CALCULATIONS

### 2.1. Experiment

The equipment used in the Sackler Laboratory for Astrophysics (SLA) and the methodology followed in the present work are similar to those described in Bossa et al. (2012, 2014) and combine mid-infrared spectroscopy (Section 2.1.1) and optical laser interferometry (Section 2.1.2). Depending on the experimental conditions, ices are grown with different morphologies, namely (i) pure and compact ices in order to obtain the reference mid-infrared optical constants, and (ii) porous composite ices in order to confront experimental and effective optical constants. Pure and compact ices are obtained by using a gas inlet (2 mm inner diameter) directed at normal incidence toward a cryogenically cooled silicon substrate, located in the center of a high-vacuum (HV) chamber ( $2 \times 10^{-7}$  Torr at room temperature). For porous composite ices (e.g.,  $\text{H}_2\text{O}:\text{CH}_4 = 10:1, 4:1, 2:1, \text{ and } 1:1$ ), a second gas inlet tube (2 mm inner diameter) is directed away from the substrate holder, which allows the gas-phase molecules to impinge on the cold surface with random trajectories, thus providing porous structures and ensuring a uniform ice growth. We define the deposition rate as the ice thickness deposited (in nanometers) per unit of time (seconds). A large-volume (2 L) gas reservoir together with an aperture-adjusted leak valve are used to always ensure a constant deposition rate ( $0.2 \text{ nm s}^{-1}$ ) in both configurations. The silicon substrate is mounted on the tip of a closed-cycle helium cryostat that, in conjunction with resistive heating, allows an accurate temperature control from 18 to 300 K with a relative precision of 0.1 K. Ices are grown at 30 K and this growth temperature is also used in the theoretical section. The gases that we use include methane ( $\text{CH}_4$ ; Praxair, purity 99.9995%) and milli-Q grade water ( $\text{H}_2\text{O}$ ) that is purified by several freeze–thaw cycles prior to deposition. The relative molecular abundances in the gas phase are obtained by a standard manometric technique with an absolute precision of 10%. The final mixing ratio in the solid phase is determined by regular infrared spectroscopy methods and by using the integrated absorption coefficients from the literature (Hagen et al. 1981; d’Hendecourt & Allamandola 1986). In order to minimize systematic errors and to understand the effect of the deposition rate, we have repeated a set of independent measurements for the pure and compact ices at LASA (Laboratório de Astroquímica e Astrobiologia da univap), located at São José dos Campos, São Paulo, Brazil. Here, ices are produced in an ultra-high-vacuum (UHV) chamber ( $1.5 \times 10^{-9}$  Torr at room temperature) from methane condensation and sublimated water, onto a zinc selenide ( $\text{ZnSe}$ ) substrate holder cooled at 30 K. The pure ice films are grown by front deposition to ensure compactness.

#### 2.1.1. Mid-infrared Spectra

Infrared spectroscopy is used after each deposition in order to extract the experimental mid-infrared optical constants of the different ice samples. Infrared spectroscopy and optical laser interferometry (Section 2.1.2) cannot be performed simultaneously because of geometrical restrictions in the HV set-up (Bossa et al. 2012, 2014; Isokoski et al. 2014). Therefore separate experiments are performed but with identical deposition procedures. For each ice sample, the same deposition procedure has been repeated up to four times and gives a mean absolute error on the deposition rate of about  $0.02 \text{ nm s}^{-1}$ .

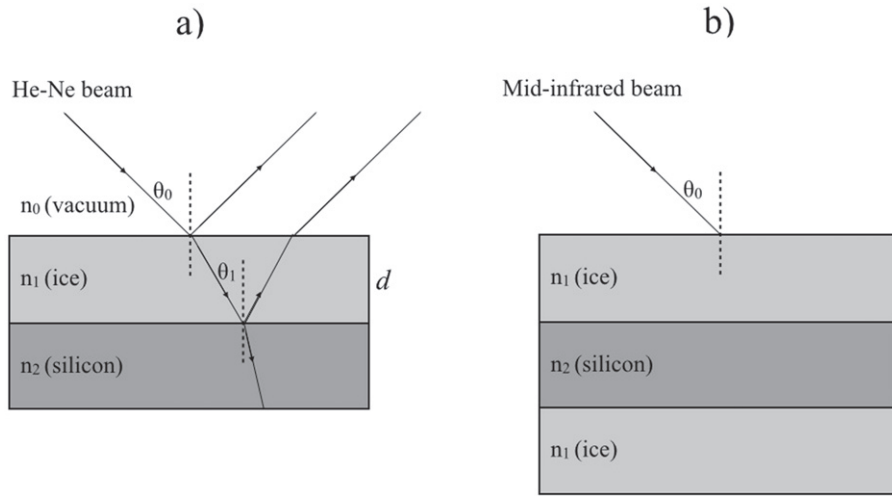


**Figure 1.** Schematic of the layered structure of the system: (a) front deposition and (b) background deposition.

Infrared spectra are obtained with two Fourier transform infrared spectrometers (Varian 670-IR FTIR in SLA and Agilent Cary 630 FTIR in LASA) and are recorded in transmission mode between 4000 and 400  $\text{cm}^{-1}$ . The infrared beam is transmitted through the ice sample and the substrate at an incident angle of  $45^\circ$  at the SLA and  $90^\circ$  at the LASA. An infrared spectrum has a  $2 \text{ cm}^{-1}$  resolution. The FTIRs are flushed with dry air to minimize background fluctuations due to atmospheric absorptions. Background spectra are acquired at the specific growth temperature prior to deposition for each experiment.

### 2.1.2. Thickness and Refractive Index Determination

The thickness and refractive index in the visible are determined with optical laser interferometry. In the SLA we use an intensity-stabilized red ( $\lambda = 632.8 \text{ nm}$ ) helium–neon (He–Ne) laser (Thorlabs HRS015). The laser beam is  $s$ -polarized (perpendicular) with respect to the plane of incidence, and strikes the substrate surface at an incident angle  $\theta_0 = 45^\circ$ . The reflected light is thereafter collected and converted to an analog signal by an amplified photodiode (Thorlabs PDA36A). The photodiode signal and the substrate temperature are recorded simultaneously as a function of time using LabVIEW 8.6 (National Instruments) at a sampling rate of 0.5 Hz. The observed signal intensity modulation with deposition time (not shown here) is due to constructive and destructive interferences (Brown et al. 1996; Westley et al. 1998; Dohnálek et al. 2003; Isokoski et al. 2014). Ice sample depositions are typically stopped when the interference signal is located on an upward slope, e.g., halfway between the third destructive interference and the third constructive interference (Bossa et al. 2012, 2014; Isokoski et al. 2014). For pure and compact ices, the thickness  $d$  can be expressed as a function of interference fringes  $m$ :

$$d = \frac{m\lambda}{2N_1/N_0 \cos \theta_1}, \quad (1)$$

where  $N_0$  and  $N_1$  are the optical constants of vacuum and ice, respectively, and  $\theta_1$  is the angle of refraction. Typical ice thicknesses are below  $1 \mu\text{m}$ . To exclude the influence of the gas deposited on the backside of the substrate, we have worked with a silicon substrate that is opaque to the He–Ne laser

wavelength. We use refractive indices  $n_0 = 1$  for vacuum,  $n_1 = 1.285$  for the pure and compact water ice (Dohnálek et al. 2003), and  $n_1 = 1.329$  for the pure and compact methane ice (Brunetto et al. 2008). We assume that the He–Ne light absorption in the relatively thin ices is negligible, so the extinction coefficients  $k_0$  and  $k_1$  equal zero. For porous composite ices, the refractive indices are unknown and need to be determined. We use a three-phase layered model (vacuum, ice, and silicon as depicted in Figure 1(a) to derive the  $n_1$  values, which depend strongly on the experimental conditions. In order to compare the different ice samples one by one and to minimize the parameters that can drastically change the final porosity, we choose a constant background deposition rate of  $0.2 \text{ nm s}^{-1}$  and a fixed growth temperature of 30 K. The total reflection coefficient  $R[d, n_1]$  can be written as a function of the Fresnel reflection coefficients according to the relation (Westley et al. 1998; Dohnálek et al. 2003; Bossa et al. 2014)

$$R[d, n_1] = \frac{r_{01} + r_{12} e^{-i2\beta}}{1 + r_{01} r_{12} e^{-i2\beta}}. \quad (2)$$

The exponential term  $\beta$  describes the phase change of the light as it passes through the ice sample of thickness  $d$ :

$$\beta = \frac{2\pi d}{\lambda} n_1 \cos \theta_1. \quad (3)$$

The Fresnel reflection coefficients  $r_{01}$  and  $r_{12}$  are associated with the vacuum/ice and ice/silicon interfaces, respectively. They are also a function of the optical constants  $N_0$  (vacuum),  $N_1$  (porous composite ice), and  $N_2$  (silicon). For  $s$ -polarized light, the Fresnel reflection coefficients are

$$r_{01s} = \frac{N_0 \cos \theta_0 - N_1 \cos \theta_1}{N_0 \cos \theta_0 + N_1 \cos \theta_1}, \quad (4)$$

$$r_{12s} = \frac{N_1 \cos \theta_1 - N_2 \cos \theta_2}{N_1 \cos \theta_1 + N_2 \cos \theta_2}. \quad (5)$$

The angles of incidence ( $\theta_0$ ,  $\theta_1$ , and  $\theta_2$ ) and the optical constants ( $N_0$ ,  $N_1$ , and  $N_2$ ) are related through Snell's law. As for pure and compact ice samples, we assume that the extinction coefficients  $k_0$  and  $k_1$  equal zero in the visible. We

**Table 1**

Comparison Between Measured and Predicted Compositions and Refractive Indices

H <sub>2</sub> O:CH <sub>4</sub>	10:1 <sup>a</sup>	4:1 <sup>a</sup>	2:1 <sup>a</sup>	1:1 <sup>a</sup>
Calculated molar fraction <sup>b</sup> (MIR)	44:1	4.7:1	1.6:1	0.8:1
Predicted molar fraction <sup>c</sup> (MG)	26:1	3.3:1	1.8:1	0.8:1
Predicted molar fraction <sup>c</sup> (BR)	33:1	3.3:1	1.9:1	0.8:1
$f_{\text{pores}}$ volume fraction (MG)	0.19	0.09	0.07	0.04
$f_{\text{H}_2\text{O}}$ volume fraction (MG)	0.76	0.60	0.48	0.31
$f_{\text{CH}_4}$ volume fraction (MG)	0.05	0.31	0.45	0.65
$f_{\text{pores}}$ volume fraction (BR)	0.19	0.09	0.08	0.04
$f_{\text{H}_2\text{O}}$ volume fraction (BR)	0.77	0.60	0.48	0.31
$f_{\text{CH}_4}$ volume fraction (BR)	0.04	0.31	0.44	0.65
Refractive index $n_1^d$ (HeNe)	1.238	1.277	1.302	1.298
Refractive index $n_1^e$ (MG)	1.232	1.272	1.284	1.302
Refractive index $n_1^e$ (BR)	1.231	1.272	1.281	1.302

**Notes.**<sup>a</sup> Expected from standard manometric technique.<sup>b</sup> Obtained from the mid-infrared (MIR) spectra and the integrated absorption coefficients available from the literature.<sup>c</sup> Deduced from the optimized volume fractions by taking into account the densities of pure and compact water and methane ices.<sup>d</sup> Measured from optical laser interferometry at  $\lambda = 632.8$  nm. For comparison, the refractive indices of pure and compact H<sub>2</sub>O and CH<sub>4</sub> ices are 1.285 (Dohnálek et al. 2003) and 1.329 (Brunetto et al. 2008), respectively.<sup>e</sup> Predicted by the extended Maxwell Garnett (MG) and Bruggeman (BR) EMA at  $\lambda = 632.8$  nm.

use  $N_2 = 3.85 - 0.07i$  for the silicon substrate (Mottier & Valette 1981). The thickness  $d$  and the  $n_1$  values result from fitting the complete interference fringe pattern to the reflectance signal  $|R[d, n_1]|^2$ . The fitting procedure is driven by Matlab 7.9.0 (R2009b), and uses the Nelder–Mead optimization algorithm (Lagarias et al. 1998). The resulting  $n_1$  values are given in Table 1.

*2.1.3. Mid-infrared Optical Constants*

In contrast to the visible range, the extinction coefficients  $k_1$  of the porous composite ices do have positive values in the mid-infrared and need to be determined together with the refractive indices  $n_1$ . Porous composite ices are grown by background deposition and this results in an ice growth on both front and backside of the substrate. Thus, the infrared beam is transmitted through both ice films and we need to take this effect into account. The experimental mid-infrared optical constants ( $N_1 = n_1^{\bar{\nu}} - ik_1^{\bar{\nu}}$ ) are determined using an analytical model of another three-phase layered model (ice, silicon, and ice as depicted in Figure 1(b)) in 45° transmission mode and are based on the Fresnel equations. A Fortran computer program implements a procedure that minimizes iteratively the difference between experimental and calculated absorption spectra for various thicknesses, employing two merit functions. A detailed description of the program and the fitting procedure is given in Zanchet et al. (2013). The transmittance  $T$  of the three-layered system (thin films deposited on both sides of a substrate as seen in Figure 1(b)) depends on several parameters

as indicated schematically in the following equation:

$$T = f(N_1, N_2, d, c, \theta_0, \bar{\nu}), \quad (6)$$

where  $N_1$  and  $N_2$  are the optical constants of the porous composite ice and the silicon,  $d$  corresponds to the ice thickness,  $c$  is the degree of coherence of the film ( $0 \leq c \leq 1$ ),  $\theta_0$  is the angle of incidence (see Figure 1(b)), and  $\bar{\nu}$  is the wavenumber of the radiation. The appropriate Fresnel coefficients, corresponding to non-normal incidence (Zanchet et al. 2013), are considered in order to calculate the transmittance of the system. We can derive a rather accurate value of the ice thickness  $d$  from optical laser interferometry (see Section 2.1.2). The accuracy of those initial values is critical to ensure success of the fitting procedure. An initial value of the extinction coefficients  $k_1^{\bar{\nu}}$  is calculated for each wavenumber using Lambert’s law for the thickest ice film:

$$k_1^{\bar{\nu}} = \frac{1}{4\pi\bar{\nu}d} A^{\bar{\nu}}, \quad (7)$$

where  $A^{\bar{\nu}}$  corresponds to the absorbance at a given wavenumber  $\bar{\nu}$ . The corresponding  $n_1^{\bar{\nu}}$  is then derived from the Kramers–Kronig equation

$$n_1^{\bar{\nu}} = n_1^{\text{HeNe}} + \frac{2}{\pi} P \int_{\bar{\nu}_1}^{\bar{\nu}_2} \frac{\bar{\nu}' k_1^{\bar{\nu}'}}{\bar{\nu}'^2 - \bar{\nu}^2} d\bar{\nu}', \quad (8)$$

where  $n_1^{\text{HeNe}}$  corresponds to the refractive index of the porous composite ice in the visible (see Section 2.1.2 and Table 1),  $\bar{\nu}_1$  and  $\bar{\nu}_2$  define the wavenumber range under consideration (1000 and 4000 cm<sup>-1</sup>) and  $P$  indicates the Cauchy principal value of the integral. Using these initial values, the optimization procedure is set to refine  $k_1^{\bar{\nu}}$  using the complete set of absorbance spectra as input data. From the improved values of the extinction coefficient  $k_1^{\bar{\nu}}$ , the refractive indices  $n_1^{\bar{\nu}}$  are estimated, and the procedure is repeated until convergence is achieved. The second step includes an adjustable baseline subtraction from each mid-infrared spectrum to correct for spectral deformations due to scattering effects, and a refinement of the corresponding coherence parameter. Next,  $n_1^{\text{HeNe}}$  and the ice film thickness  $d$  are adjusted to their final values, and last, the final refined set of  $n_1^{\bar{\nu}}$  and  $k_1^{\bar{\nu}}$  values is obtained.

We have applied this procedure to three porous composite ices (H<sub>2</sub>O:CH<sub>4</sub> = 4:1, 2:1, and 1:1). Four, six, and four mid-infrared spectra with thicknesses below 1 μm are fitted for each ratio. The initial  $n_1^{\text{HeNe}}$  values taken are 1.277, 1.302, and 1.298 for the three mixtures, respectively. All refined values for thicknesses  $d$  and refractive indices in the visible  $n_1^{\text{HeNe}}$  agree with their experimental determinations within their estimated 0.4% uncertainties. We tried to apply this same procedure to obtain the optical constants of pure and compact H<sub>2</sub>O and CH<sub>4</sub> ices. However, ice films grown by front deposition have an inhomogeneous thickness (pyramidal shape) that somehow modifies the mid-infrared interference fringes in the spectra and prevents their use for spectral reproduction. Hence, for pure and compact H<sub>2</sub>O and CH<sub>4</sub> ices, we use a different approach previously applied by other groups (Mastrapa et al. 2008; Zanchet et al. 2013; Rocha & Pilling 2014). First, an adequate baseline is subtracted from the spectra. Then,  $k_1^{\bar{\nu}}$  is calculated using Equation (7) and the values obtained from different ice thicknesses are averaged. The final  $k_1^{\bar{\nu}}$  is then used to derive  $n_1^{\bar{\nu}}$

via the Kramers–Kronig relationship given in Equation (8) with  $n_1^{\text{HeNe}} = 1.285$  for the pure and compact water ice, and  $n_1^{\text{HeNe}} = 1.329$  for the pure and compact methane ice (see Section 2.1.2). This same method is used to obtain the mid-infrared optical constants of a fourth mixture ( $\text{H}_2\text{O}:\text{CH}_4 = 10:1$ ), as for this setting only one spectrum was recorded.

## 2.2. Theory

### 2.2.1. Effective Mid-infrared Optical Constants

In this section we visualize a porous  $\text{H}_2\text{O}:\text{CH}_4$  ice sample as a heterogeneous material, i.e., three different dielectric materials compose the ice sample: pores, water, and methane. We assume that the constituents do not strongly interact with each other. Previous studies focused on extended EMAs with the aim of predicting the effective optical constants of three-component systems (Wachniewski & McClung 1986; Jayanavar & Kumar 1991; Nicorovici et al. 1995; Luo 1997). We have recently demonstrated that optical laser interferometry combined with extended EMAs can provide a tool for measuring the porosity of ice mixtures grown by background deposition (Bossa et al. 2014). This was achieved by using a non-absorbing monochromatic light source in the visible. In this study, we extend the same approach to the mid-infrared region (4000–1000  $\text{cm}^{-1}$  with a 2  $\text{cm}^{-1}$  resolution). The ice composition is determined by another fitting procedure driven by Matlab 7.9.0 (R2009b). The parameter optimization proceeds by minimizing over  $1501 \times 2$  data points, the sum of squared differences (SSD) between the effective mid-infrared optical constants ( $n_{\text{eff}}^{\bar{\nu}} - ik_{\text{eff}}^{\bar{\nu}}$ ) and the experimental mid-infrared optical constants ( $n_1^{\bar{\nu}} - ik_1^{\bar{\nu}}$ ) obtained in Section 2.1.3:

$$\begin{aligned} \text{SSD} &= \Delta n^2 + \Delta k^2 \\ &= \sum_{\bar{\nu}_1}^{\bar{\nu}_2} (n_{\text{eff}}^{\bar{\nu}} - n_1^{\bar{\nu}})^2 + \sum_{\bar{\nu}_1}^{\bar{\nu}_2} (k_{\text{eff}}^{\bar{\nu}} - k_1^{\bar{\nu}})^2. \end{aligned} \quad (9)$$

The parameters to optimize are the volume fractions  $f$  of the three different constituents that compose the porous ice mixture. The methodology we followed in order to obtain the different effective mid-infrared optical constants ( $n_{\text{eff}}^{\bar{\nu}} - ik_{\text{eff}}^{\bar{\nu}}$ ) as a function of ice composition is thoroughly described in the Appendix (extended Maxwell Garnett and Bruggeman EMAs). Considering a volume fraction resolution of 0.01, we calculated 4851 cases that satisfy  $\sum f = 1$ . Therefore, the resulting minimum solving Equation (9) is considered to be the global minimum at a given volume fraction resolution.

### 2.2.2. Dependence of Porosity on Deposition Rate: Monte Carlo Simulation

We use a step-by-step Monte Carlo simulation to follow the growth of pure water ice at 30 K as well as the pore evolution within the bulk during deposition. The model has been described in Cazaux et al. (2015). In order to model amorphous solid water, we use a grid with predefined host sites for water molecules that allows a tetrahedral hydrogen bonding structure. Water molecules originating from the gas phase arrive at a random time and location, migrate following a random path within the grid, and eventually form hydrogen bonds with water molecules already present. The accretion rate,  $R_{\text{acc}}$  in  $\text{s}^{-1}$ ,

depends on the velocity of the impinging species, their density, and the cross section of the surface:

$$R_{\text{acc}} = V_{\text{H}_2\text{O}} S \sigma n_{\text{H}_2\text{O}}, \quad (10)$$

where  $V_{\text{H}_2\text{O}} \sim 0.43 \times 10^5 \sqrt{\frac{T_{\text{gas}}}{100 \text{ K}}} \text{ km s}^{-1}$  is the thermal velocity and  $S$  corresponds to the sticking coefficient that we consider to be unity for the low temperature taken as a starting point in this study. The cross section of the surface,  $\sigma$  in  $\text{cm}^2$ , directly scales with the size of the grid that we use during the simulation, which is typically  $100 \times 100$  sites. This corresponds to a size of  $(1.58 \times 10^{-8} \times 100)^2 \text{ cm}^2$ , since the distance between two sites is 1.58 Å. The accretion rate is therefore  $R_{\text{acc}} = 1.86 \times 10^{-7} \times n_{\text{H}_2\text{O}} \text{ s}^{-1}$ . In order to mimic the experimental conditions with deposition rates of 0.2 and 10  $\text{nm s}^{-1}$ , we set the density of water molecules in the gas phase to be  $n_{\text{H}_2\text{O}} = 4 \times 10^9 \text{ cm}^{-3}$  and  $n_{\text{H}_2\text{O}} = 2 \times 10^{11} \text{ cm}^{-3}$ , respectively. As assumed in our previous simulations, the binding energy of a water molecule is estimated at 0.22 eV per hydrogen bond and increases with the number of neighbors (Brill & Tippe 1967; Isaacs et al. 1999; Dartois et al. 2013). We assume that the binding energy increases linearly with the number of neighbors, so that water molecules surrounded by one neighbor have a binding energy of 0.22 eV and water molecules surrounded by four neighbors (maximum) have a binding energy of 0.88 eV. The diffusion rate,  $\alpha(m)$  in  $\text{s}^{-1}$ , of a water molecule with  $m$  neighbors is defined as following

$$\alpha(m) = \nu \exp\left[\frac{-nmE_{\text{diff}}}{T}\right], \quad (11)$$

where  $\nu$  is the vibrational frequency of a water molecule on a site, which we set to  $10^{12} \text{ s}^{-1}$ ,  $T$  corresponds to the temperature of the growing ice (30 K),  $E_{\text{diff}}$  defines the diffusion of water molecules, which is proportional to the energy of a single hydrogen bond (0.22 eV or 2553 K), and  $nm$  is the total number of neighbors.

## 3. RESULTS AND DISCUSSION

Accurate reference optical constants are required for determinations of effective optical constants of different porous composite ices. To the best of our knowledge, there exist no values in the literature for both the deposition rate and growth temperature of interest here. Therefore, we have deposited our pure and compact ices as references, then we have extracted from their mid-infrared spectra the corresponding (intrinsic) optical constants following the methodology described in Section 2.1.3. No attempts have been made to analyze the effect of growth temperature. However, we have investigated the reproducibility at a faster deposition rate (10  $\text{nm s}^{-1}$ ) because it is expected that a higher deposition rate comes with more disordered structures (Maté et al. 2012).

### 3.1. Mid-infrared Spectra

Pure and compact  $\text{H}_2\text{O}$  and  $\text{CH}_4$  ices are grown by front deposition at 30 K with two different constant deposition rates. Figure 2(a) shows the mid-infrared spectra of pure methane ices grown at 0.2  $\text{nm s}^{-1}$  (SLA) and 10  $\text{nm s}^{-1}$  (LASA). In this case, the two deposition rates result in ice films with very similar spectra that are characteristic of the crystalline phase I

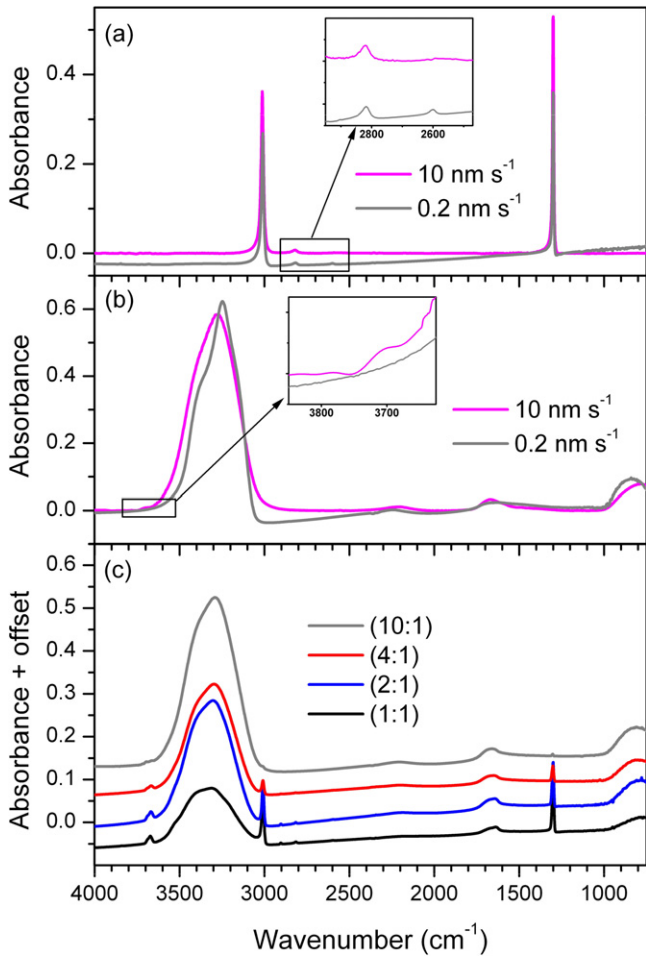


**Figure 2.** Mid-infrared spectra of (a) pure and compact CH<sub>4</sub> ice grown at 30 K (0.4 μm, front deposition) using two different deposition rates, (b) pure and compact H<sub>2</sub>O ice grown at 30 K (0.6 μm, front deposition) with two different deposition rates, and (c) porous H<sub>2</sub>O:CH<sub>4</sub> ice mixtures grown at 30 K (0.4 μm, background deposition) with a 0.2 nm s<sup>-1</sup> deposition rate.

of methane (Hudson et al. 2015 and references therein). The only noticeable difference, highlighted in the inset, is an intensification of the 2600 cm<sup>-1</sup> band assigned to the 2ν<sub>4</sub> mode (Baciocco et al. 1987) observed in the methane ice spectrum grown at the lowest rate. The pure water ice spectra are presented in Figure 2(b). Here, clear spectral differences are found between the two ice samples grown at different deposition rates, mainly in the regions of the bulk O–H stretching (3280 cm<sup>-1</sup>) and the libration (780 cm<sup>-1</sup>) modes. The spectrum of the water ice grown at 0.2 nm s<sup>-1</sup> shows that the O–H stretching band is narrowed and slightly redshifted compared to the measurement with a 10 nm s<sup>-1</sup> deposition rate. Moreover, no trace of the O–H dangling modes is present (see inset). This behavior points to a more compact ice than the one grown with a 10 nm s<sup>-1</sup> deposition rate (Zondlo et al. 1997; Maté et al. 2012). Figure 2(c) depicts the four mid-infrared spectra of the different porous H<sub>2</sub>O:CH<sub>4</sub> ice mixtures investigated in this work. All samples are grown by background deposition at 30 K with a 0.2 nm s<sup>-1</sup> deposition rate in order to obtain porous structures (Dohnálek et al. 2003; Bossa et al. 2012). In contrast to the case of pure and compact H<sub>2</sub>O ices (Figure 2(b)), we observe here that the O–H dangling bond features are present (3720 and 3696 cm<sup>-1</sup>) with relatively high intensities. The most intense O–H dangling bonds are found in

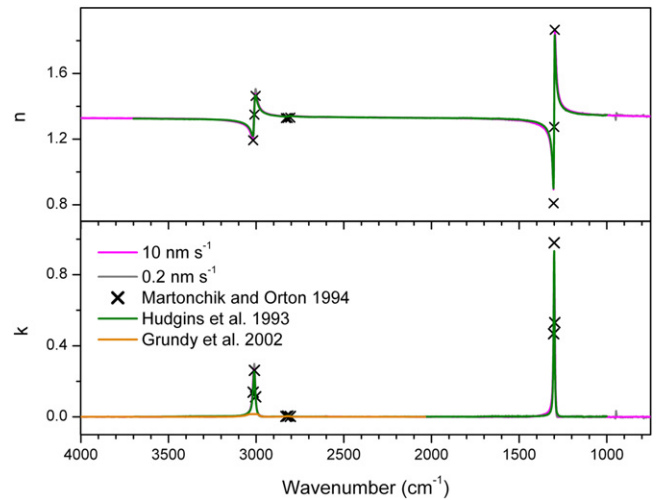


**Figure 3.** Experimental mid-infrared optical constants of pure and compact CH<sub>4</sub> ice grown at 30 K (front deposition) using two different deposition rates (10 nm s<sup>-1</sup> in magenta and 0.2 nm s<sup>-1</sup> in gray) compared with the data available from the literature.

the 1:1 mixture. However, as will be discussed later, the intensity of the O–H dangling bonds is not directly related to the level of porosity of the ice sample. Finally, we observe in the 2:1 and 1:1 ratios, the forbidden ν<sub>1</sub> symmetric stretching vibration (breathing mode) of methane around 2902 cm<sup>-1</sup> (Hodyss et al. 2009; Escribano et al. 2014). We do not observe this very weak feature in the spectra recorded for the 10:1 and 4:1 ratios, most likely due to the too low methane concentration. Activation of this forbidden mode is attributed to the interaction of a methane molecule and a water molecule on the internal surface of a pore (Escribano et al. 2014). This forbidden mode is also known to be enhanced when pure CH<sub>4</sub> is amorphous, while it is barely visible in crystalline solids (Hudson et al. 2015).

### 3.2. Mid-infrared Optical Constants

The experimental mid-infrared optical constants ( $n_1^p - ik_1^p$ ) are determined between 4000 and 1000 cm<sup>-1</sup> from the spectra of the pure and compact ices and the spectra of the porous ice mixtures. Below 1000 cm<sup>-1</sup>, the libration mode of water becomes difficult to fit because its band profile strongly depends on the environment (Öberg et al. 2007). Therefore, we choose to exclude all data below this threshold. An iterative procedure described in Section 2.1.3 is applied for the porous H<sub>2</sub>O:CH<sub>4</sub> = 4:1, 2:1, and 1:1 ice mixtures. For the pure and compact ices and for the porous H<sub>2</sub>O:CH<sub>4</sub> = 10:1 ice mixture, we followed a different approach as explained above.

Figure 3 presents the wavelength-dependent refractive indices (upper panel) and extinction coefficients (lower panel) of pure and compact CH<sub>4</sub> ice grown at 30 K using 0.2 nm and 10 nm s<sup>-1</sup> deposition rates. These values are compared with those found in the literature (Hudgins et al. 1993; Martonchik & Orton 1994; Grundy et al. 2002) and we observe an excellent match between them. Hudgins and coworkers determined their optical constants from a 30 nm thick ice, deposited at 10 K by vapor deposition at a 1.5 nm s<sup>-1</sup> deposition rate and then warmed to 30 K. The corresponding ice layer, however, is too thin to observe the weak 2ν<sub>4</sub> mode. Martonchik and Orton refer to ices grown at 15 K and then heated to 33 K. The authors only provide a limited data set close to the strongest absorption

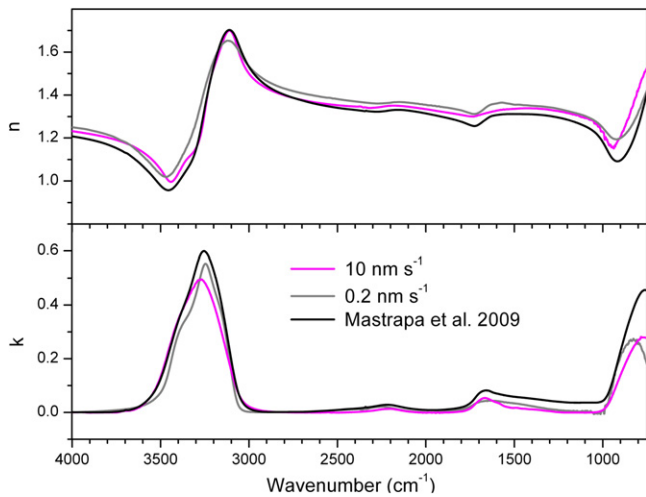


**Figure 4.** Experimental mid-infrared optical constants of pure and compact  $\text{H}_2\text{O}$  ice grown at 30 K (front deposition) using two different deposition rates ( $10 \text{ nm s}^{-1}$  in magenta and  $0.2 \text{ nm s}^{-1}$  in gray) compared with the data available from the literature.

features. In the study of Grundy and coworkers, the optical constants arise from a single crystal generated by freezing liquid-phase methane. The authors obtain a very thick ice sample, allowing the weak  $2600 \text{ cm}^{-1}$  absorption band to be observed. This is in good agreement with the one observed in the pure and compact methane ice spectra grown at 30 K with a  $0.2 \text{ nm s}^{-1}$  deposition rate. Figure 4 compares the optical constants obtained in this work for the pure and compact water ices using different deposition rates with those reported by Mastrapa et al. (2009). They studied amorphous solid water grown at 30 K by background deposition with a  $5 \text{ nm s}^{-1}$  deposition rate. An overall agreement is observed, although differences in shape and intensity can be noticed, which may be attributed, apart from differences in deposition rate, to differences in ice morphology. Figure 5 displays the experimental optical constants obtained for the porous  $\text{H}_2\text{O}:\text{CH}_4 = 10:1, 4:1, 2:1,$  and  $1:1$  ice mixtures. Up to six mid-infrared spectra with different thicknesses below  $1 \mu\text{m}$  are fitted iteratively to obtain the optical constants, except the  $\text{H}_2\text{O}:\text{CH}_4 = 10:1$  ratio for which a less accurate procedure is employed. As far as we know, there are no reference data in the literature for a direct comparison. However, it should be noted that a one-to-one comparison is only useful for porous  $\text{H}_2\text{O}:\text{CH}_4$  ice mixtures showing a comparable composition and morphology. For the four mixtures studied here, substantial differences can already be observed in both  $n$  and  $k$  values at several wavelengths, mainly due to the difference in ice composition that modifies the morphology of the ice during its growth (Bossa et al. 2014). We expect that these discrepancies are large enough so they can be used to benchmark procedure detailed in Section 2.2.1. This directly confronts experimental mid-infrared optical constants with the effective mid-infrared optical constants of fictive composite ices.

### 3.3. Ice Composition and Porosity

Figure 6 shows an example of a comparison between the experimental mid-infrared optical constants obtained for a porous  $\text{H}_2\text{O}:\text{CH}_4 = 4:1$  ice mixture (black solid line) and the effective mid-infrared optical constants (best fit, red solid line). The global minimum found from the fit gives a predicted

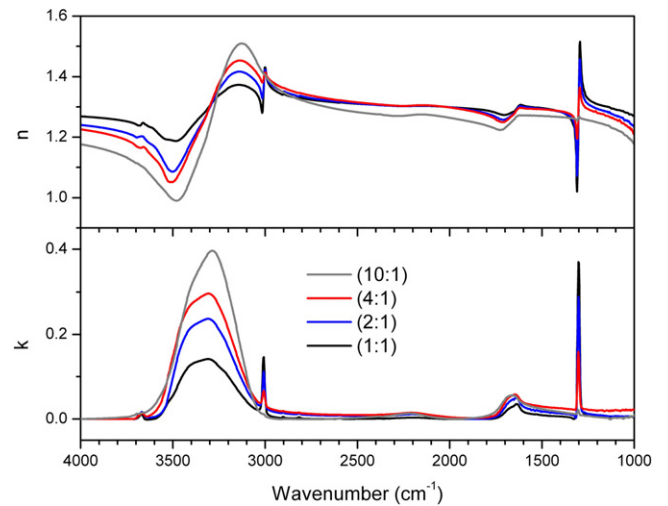


**Figure 5.** Experimental mid-infrared optical constants of porous  $\text{H}_2\text{O}:\text{CH}_4 = 10:1, 4:1, 2:1,$  and  $1:1$  ice mixtures, grown at 30 K (background deposition) with a  $0.2 \text{ nm s}^{-1}$  deposition rate.

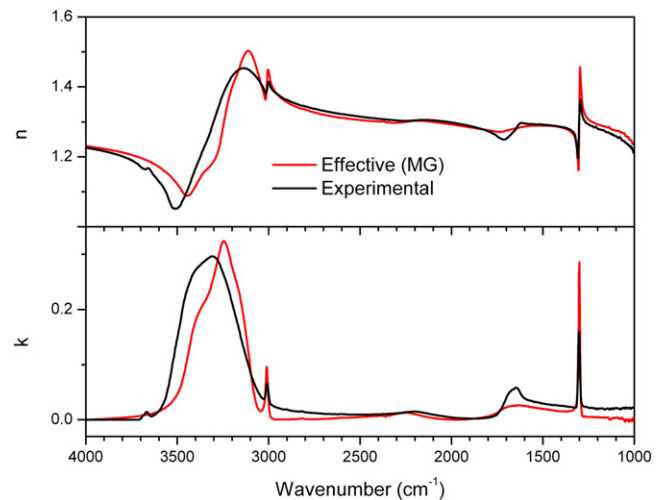


**Figure 6.** Experimental vs. effective mid-infrared optical constants obtained for a  $\text{H}_2\text{O}:\text{CH}_4 = 4:1$  ice grown at 30 K (background deposition) with a  $0.2 \text{ nm s}^{-1}$  deposition rate. The red solid line corresponds to the best fit obtained from the extended Maxwell Garnett (MG) EMA. The global minimum gives a predicted volume fraction of pores, water, and methane of 0.09, 0.60, and 0.31, respectively.

volume fraction  $f$  of pores, water, and methane of 0.09, 0.60, and 0.31, respectively. The optimized effective mid-infrared optical constants ( $n_{\text{eff}}^{\nu} - ik_{\text{eff}}^{\nu}$ ) are fairly similar to the measurements, except for the  $3800\text{--}3000 \text{ cm}^{-1}$  range that covers the O–H dangling and the bulk O–H stretching modes of water. The extinction coefficients  $k_{\text{eff}}^{\nu}$  related to the  $\text{H}_2\text{O}$  bending mode around  $1650 \text{ cm}^{-1}$  are slightly reduced whereas those of the stretching and bending modes of methane around  $3010$  and  $1302 \text{ cm}^{-1}$  are slightly enhanced. Note that the largest differences correspond to less than 30% of the whole data set. The optical constants related to the O–H dangling modes cannot be reproduced accurately by the two extended EMAs used here simply because they are not present in the reference optical constants of the pure and compact water ice. Therefore, the  $3710\text{--}3640 \text{ cm}^{-1}$  region cannot be trusted for a proper fit. In general, EMAs cannot predict the influence of new products or strong interactions between constituents

(Mukai et al. 1987). As noted in a previous study, the band profile of the bulk O–H stretching mode only shows subtle changes when a contaminant (in this case CO<sub>2</sub>) is added (Öberg et al. 2007). Thus, the observed changes in shape and position can only be explained by the difference in morphology between the compact water ice taken as a reference and the porous composite ice. The bulk O–H stretching mode provides a direct probe of different coupling mechanisms and reveals characteristic substructures that can affect the line shape. Since this mode is very sensitive to its local environment, the assignment of the multiple peaks and shoulders that constitute the strong absorption feature remains a challenging problem, especially when morphology disorder is added (Perakis & Hamm 2012). These new and strong interactions that alter the shape of the bulk O–H stretching band show the limitations of the extended EMAs in predicting reasonable optical constants in this region. The models are therefore more accurate when the composite material retains as far as possible the features of the pure constituents. Taking into account these limitations and the misfits observed in some parts of the mid-infrared spectra, the outcomes of the fitting procedure are further tested in the following.

Since a direct experimental measurement of the porosity cannot be performed, the relative molecular abundances obtained from the standard manometric technique and the mid-infrared spectra are used as reference points. Thus, we can only test the optimized volume fractions  $f_{\text{H}_2\text{O}}$  and  $f_{\text{CH}_4}$ . For the reference points, we focus on the 3800–2950 cm<sup>-1</sup> range that covers the O–H dangling and the bulk O–H stretching modes ( $A_{\text{H}_2\text{O}} = 2.0 \times 10^{-16}$  cm molecule<sup>-1</sup>) of water (Hagen et al. 1981; d’Hendecourt & Allamandola 1986) and the C–H stretching mode of methane ( $A_{\text{CH}_4} = 6.4 \times 10^{-18}$  cm molecule<sup>-1</sup>) (d’Hendecourt & Allamandola 1986). These  $A$ -values are commonly used in the literature. Due to overlapping features, the O–H dangling modes and the C–H stretching mode are removed and replaced by one polynomial function; all spectra are then corrected with a baseline (not shown here). The molar fractions deduced from the mid-infrared spectra are listed in Table 1. For the expected H<sub>2</sub>O:CH<sub>4</sub> = 4:1 ratio in the gas mixing line, a final ratio H<sub>2</sub>O:CH<sub>4</sub> = 4.7:1 is found in the solid phase at 30 K. In general, we observe that for the most concentrated mixtures, the final solid-phase ratio is rather close to the expected gas-phase ratio. The discrepancy gets larger with increasing water dilution. This can be explained by various fractionation effects from the gas mixing line, through tubes and valves, to the cold silicon substrate. In addition, band strengths are known to be dependent on the ice composition (Öberg et al. 2007), thus larger uncertainties may arise together with water dilution when constant  $A$ -values are used. Finally, the most diluted mixture provides weak methane absorption features, inducing larger uncertainties during the methane band integration procedure. Molar fractions can be deduced in a second step by taking into account the densities of pure and compact water and methane ices: 0.94 and 0.47 g cm<sup>-3</sup>, respectively (Dohnálek et al. 2003; Satorre et al. 2008). The molar fractions deduced from the optimized volume fractions are compared in Table 1. The striking similarities between the experimental molar fractions and the predicted molar fractions provide the first experimental evidence that extended EMAs can predict the composition of porous composite ices dominated by water. We have also calculated the effective refractive indices  $n_1$  at  $\lambda = 632.8$  nm, using the optimized

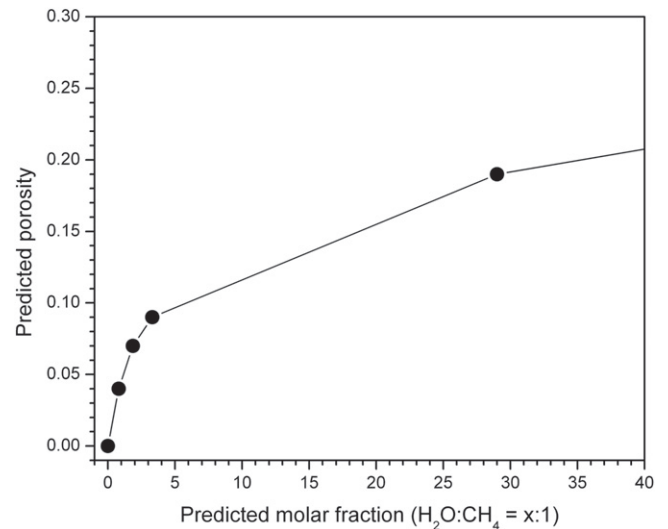


**Figure 7.** Predicted porosity after background deposition at 30 K with a 0.2 nm s<sup>-1</sup> deposition rate as a function of predicted molar fraction, following the extended Maxwell Garnett and Bruggeman EMAs. The solid line is drawn to guide the eye.

volume fractions obtained by the fitting procedure in the mid-infrared as input for the extended EMAs in the visible (Bossa et al. 2014). We found an excellent agreement with the values measured independently from optical laser interferometry. At this stage, the largest difference (1.5%) observed for the H<sub>2</sub>O:CH<sub>4</sub> = 2:1 ratio cannot be explained. As seen previously for porosity measurements in the visible, the extended Maxwell Garnett EMA predictions are similar to those of the extended Bruggeman EMA (Bossa et al. 2014). Most heterogeneous materials can be approximated by the two presented EMAs (Niklasson et al. 1981). In general, the Maxwell Garnett EMA is expected to be valid with inclusions (e.g., pores) occupying low volume fractions, and the Bruggeman EMA is frequently used to describe both surface roughness and porosity. Therefore, it is not surprising that for low predicted porosity, ranging from 4% to 19%, extended Maxwell Garnett and Bruggeman EMAs give very similar results.

Figure 7 shows the predicted porosity after background deposition at 30 K with a 0.2 nm s<sup>-1</sup> deposition rate as a function of predicted molar fractions. The solid line is drawn to guide the eye. We assume a fully compact methane ice when there is no water and we expect an asymptotic value of around 30% porosity when pure water ice is deposited by background deposition (Bossa et al. 2014). In general, we observe that the predicted porosity decreases when the methane concentration increases. We have observed a similar trend in the visible range, when carbon dioxide (CO<sub>2</sub>) was premixed with water, in the specific case where the physical conditions favorable to CO<sub>2</sub> segregation were reached (Bossa et al. 2014). There is no mid-infrared signature of CH<sub>4</sub> segregation, but it is very likely that a similar mechanism proposed for CO<sub>2</sub> applies also for the CH<sub>4</sub> molecules that could readily diffuse at 30 K onto the surface of the growing ice sample prior to being incorporated into the bulk, then filling the pores partly or completely, depending on the relative abundance of CH<sub>4</sub> in the composite ice. Finally, it is important to stress that we do not find any correlation between the intensity/area of the O–H dangling bonds and the predicted porosity, thus reinforcing the claim

**Table 2**  
Densities and Band Strengths of Pure and Porous Ice Mixtures

H <sub>2</sub> O:CH <sub>4</sub>	Pure	10:1 <sup>a</sup>	4:1 <sup>a</sup>	2:1 <sup>a</sup>	1:1 <sup>a</sup>
$\rho_{\text{H}_2\text{O}}$ ( $10^{22}$ molecules cm <sup>-3</sup> )	3.14 <sup>b</sup>	2.39	1.89	1.51	0.97
$\rho_{\text{CH}_4}$ ( $10^{22}$ molecules cm <sup>-3</sup> )	1.77 <sup>c</sup>	0.09	0.55	0.80	1.15
$A_{\text{H}_2\text{O,dangling}}$ ( $10^{-18}$ cm molecule <sup>-1</sup> )	...	0.23	0.76	1.35	1.55
$A_{\text{H}_2\text{O,stretching}}$ ( $10^{-16}$ cm molecule <sup>-1</sup> )	1.92	2.22	2.15	2.05	2.00
$A_{\text{H}_2\text{O,bending}}$ ( $10^{-18}$ cm molecule <sup>-1</sup> )	5.2	5.9	7.5	8.0	8.1
$A_{\text{CH}_4,stretching}$ ( $10^{-18}$ cm molecule <sup>-1</sup> )	14.7	2.7	3.7	5.7	6.4
$A_{\text{CH}_4,bending}$ ( $10^{-18}$ cm molecule <sup>-1</sup> )	10.1	1.8	5.1	7.4	7.1
$A_{\text{mixture}}/A_{\text{pure H}_2\text{O,stretching}}$ ( $10^{-16}$ cm molecule <sup>-1</sup> )	1	1.16	1.12	1.07	1.04
$A_{\text{mixture}}/A_{\text{pure H}_2\text{O,bending}}$ ( $10^{-16}$ cm molecule <sup>-1</sup> )	1	1.13	1.44	1.54	1.56
$A_{\text{mixture}}/A_{\text{pure CH}_4,stretching}$ ( $10^{-18}$ cm molecule <sup>-1</sup> )	1	0.18	0.25	0.39	0.44
$A_{\text{mixture}}/A_{\text{pure CH}_4,bending}$ ( $10^{-18}$ cm molecule <sup>-1</sup> )	1	0.18	0.51	0.73	0.70

**Notes.**

<sup>a</sup> Expected from standard manometric technique.

<sup>b</sup> Deduced from the density  $\rho_{\text{H}_2\text{O}} = 0.94 \text{ g cm}^{-3}$  (Dohnálek et al. 2003).

<sup>c</sup> Deduced from the density  $\rho_{\text{CH}_4} = 0.47 \text{ g cm}^{-3}$  (Satorre et al. 2008).

that the O–H dangling modes are poor probes to quantify the degree of porosity of porous ice samples dominated by water.

### 3.4. Band strengths

Accurate solid state optical constants are much needed for unravelling both interstellar and planetary chemistry, mainly for determinations of ice abundances in the outer solar system and the interstellar medium (Hudson et al. 2014). Band strengths, i.e., the  $A$ -values written in units of cm molecule<sup>-1</sup>, are even more critically required since they allow the determination of column densities from both astronomical and laboratory spectra. We have calculated the band strengths for the mid-infrared absorption features of H<sub>2</sub>O and CH<sub>4</sub> in the four porous composite ices studied here (H<sub>2</sub>O:CH<sub>4</sub> = 10:1, 4:1, 2:1, and 1:1) using the experimental extinction coefficients  $k_1^{\bar{\nu}}$  by means of the expression

$$A = \frac{4\pi}{\rho} \int k_1^{\bar{\nu}} \bar{\nu} d\bar{\nu} \quad (12)$$

where  $\rho$  is the number of absorbing molecules per unit of volume. We use  $\rho_{\text{H}_2\text{O}} = 3.14 \times 10^{22}$  and  $\rho_{\text{CH}_4} = 1.77 \times 10^{22}$  molecules cm<sup>-3</sup>. The band strengths estimated for pure and compact H<sub>2</sub>O and CH<sub>4</sub> ices are listed in Table 2 and we observe an excellent agreement with the recent (corrected) values given in the literature (Bouilloud et al. 2015), thus validating our methodology. We can only note a small offset in the band strength of the bending mode of water near 1655 cm<sup>-1</sup>. This can be explained by the use of shorter integration bounds than those typically taken in the literature due to the presence of the bending mode of methane located around 1300 cm<sup>-1</sup> in our spectra. However, some noticeable deviations (30%) are observed with the initial and commonly used band strengths of the methane features (d’Hendecourt & Allamandola 1986). In the case of the porous ice mixtures, the density is unknown but

we can estimate an average density  $\rho_{\text{H}_2\text{O:CH}_4}$  by taking into account the densities of pure and compact H<sub>2</sub>O and CH<sub>4</sub> ices, weighted by the optimized volume fractions  $f_{\text{H}_2\text{O}}$  and  $f_{\text{CH}_4}$  obtained after using the fitting procedure described above. The corresponding  $A$ - and  $\rho$ -values are also listed in Table 2 for comparison. The band strength relative to the bulk O–H stretching mode of water is the one less affected by the presence of the other constituents. Indeed, the corresponding  $A$ -value is comparable to the one obtained with the H<sub>2</sub>O:CH<sub>4</sub> = 1:1 mixture, so the presence of methane—even at the highest concentration—has almost no effect on this mode. However, a continuous but small increase in the  $A$ -value is observed with increasing predicted porosities, reaching about 10% for the most porous mixture compared to the pure and compact water ice. Therefore, we conclude that the presence of pores has only a small effect on the bulk O–H stretching mode. In contrast, the H<sub>2</sub>O bending mode is more affected by the change in ice composition. It is important to note that this mode also overlaps with the water librational overtone (Devlin et al. 2001) and its fundamental mode’s band profile strongly depends on the environment (Öberg et al. 2007). Therefore, it is very likely that the band strength of the H<sub>2</sub>O bending mode strongly depends on the methane concentration. The band strengths of the two methane features are the most affected by the presence of both water and pores. The  $A$ -values related to the C–H stretching and CH<sub>4</sub> bending modes undergo considerable attenuations with water dilution as seen previously in the literature (Hudgins et al. 1993). However, it is difficult to evaluate the impact of porosity for the band strength of these two features. An ongoing theoretical study on the mid-infrared band strengths of the methane modes suggests that an enhancement of the dielectric constant of the medium (e.g., adding water) increases the  $A$ -values, whereas lowering the dielectric constant of the medium

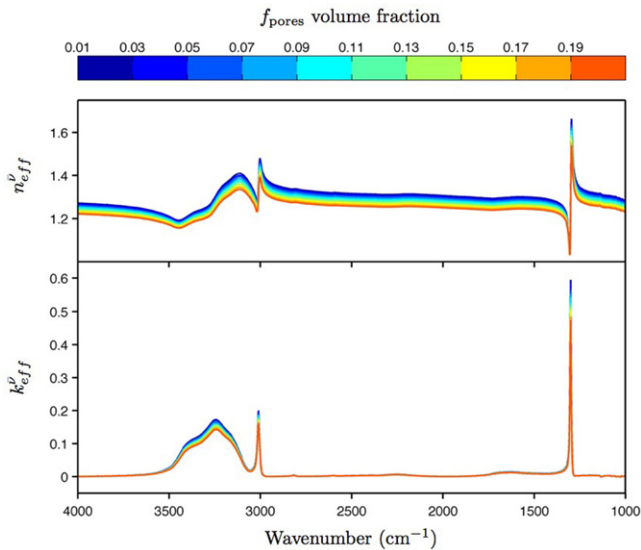


**Figure 8.** Effective mid-infrared optical constants calculated for fictive porous  $\text{H}_2\text{O}:\text{CH}_4 = 1:1$  ice mixtures with different levels of porosity ranging from 1% to 19%.

(e.g., adding pores) decreases the  $A$ -values (V. S. Bonfim & S. Pilling 2015, in preparation). This is in good agreement with the values presented in Tables 1 and 2. Figure 8 shows the effective mid-infrared optical constants calculated for fictive porous  $\text{H}_2\text{O}:\text{CH}_4 = 1:1$  ice mixtures with different levels of porosity ranging from 1% to 19%. Since we assume that pores are not absorbing light in the mid-infrared, the volume fraction of pores should have more impact on refractive indices than on the extinction coefficients. This is in good agreement with the theoretical results presented in Figure 8. Therefore, we can assume that the presence of pores at higher water dilution does not strongly affect the overall band strengths.

### 3.5. Porosity and Deposition Rate

In order to reproduce the different ice morphologies obtained with deposition rates of 10 and  $0.2 \text{ nm s}^{-1}$ , we performed several simulations with different values of  $E_{\text{diff}}$  (Equation (11)), which determines the diffusion of water molecules. For values of  $E_{\text{diff}} = 0.4 \times 0.22 \text{ eV}$ , which means that the diffusion energy equals 40% of the binding energy, the diffusion is actually too slow to allow a reorganization of water molecules at the lowest deposition rate. This means that the water ice morphology at low and high deposition rate is identical. However, for  $E_{\text{diff}} = 0.15 \times 0.22 \text{ eV}$ , the reorganization of water molecules at the lowest deposition rate is possible, hence allowing us to derive constraints on their mobility. The ice morphologies obtained for 10 and  $0.2 \text{ nm s}^{-1}$  deposition rates are depicted in Figure 9. Figure 9 also shows the position of each water molecule (colored dot) within the grid and the corresponding number of hydrogen bonds with a color code. Water molecules with one neighbor are represented in blue, while water molecules with 2, 3, and 4 neighbors are represented in green, yellow, and red, respectively. In the case of the lowest deposition rate (right panel), we observe that a substantial number of water molecules

are bonded to three and four neighbors as seen with the dominant yellow and red colors. In contrast, the highest deposition rate (left panel) exhibits a structure in which water molecules with 1 and 2 neighbors (blue and green colors) are predominant. With a  $0.2 \text{ nm s}^{-1}$  deposition rate, water molecules have more time to diffuse onto the surface, rearrange, and form hydrogen bonds than with a  $10 \text{ nm s}^{-1}$  deposition rate. Therefore, water molecules that can reorganize result also in a final ice structure dominated by hydrogen-bonded molecules. The time for a water molecule to diffuse depends on the number of neighbors (see also Equation (11)) and it is of the order of  $3.5 \times 10^{-7}$ , 0.12, and  $4.2 \times 10^4 \text{ s}$  for molecules bonded with 1, 2, and 3 neighbors, respectively. As an example, with a  $0.2 \text{ nm s}^{-1}$  deposition rate, one monolayer is deposited in 0.79 s, whereas it takes 0.016 s with a deposition rate of  $10 \text{ nm s}^{-1}$ . Therefore, the deposition rate is an important parameter that determines whether water molecules can reorganize or not, and thus whether hydrogen bondings are abundant or not.

Since we are also interested in the porosity of the ices grown with the two deposition rates investigated here, we performed a quantitative study on the size of the pores after deposition. To do so, we tag every empty grid space with a number that corresponds to the number of grid cells around this cell that are empty. In our simulations, these tags can range from 0, i.e., an empty spot with at least one water molecule as a neighbor, to 6 that is an empty spot with no water molecule present for a distance of six grid cells around, i.e., this means that the hole is the center of a sphere with a radius six grid cells. This provides a direct measurement of the total pore volume, the total surface area, and the individual pore volume. The pores and their distribution obtained with the deposition rates of 10 and  $0.2 \text{ nm s}^{-1}$  are presented in Figure 10. This figure shows pores (colored dots) with a color code as an indication of pore size and can also be seen as a negative image of Figure 9. Pores for which no water molecule is present at a radius of 2 grid cells around are represented in blue, while bigger pores with a radius of 3, 4, and 5 empty grid cells are represented in green, yellow, and red, respectively. In the case of the lowest deposition rate (right panel), the water ice is more compact and composed of fewer but larger pores compared to the highest deposition rate (left panel) for which the resulting water ice is more porous and composed of numerous smaller pores. The size of the pores can reach radii of  $\sim 14 \text{ \AA}$  with the  $0.2 \text{ nm s}^{-1}$  deposition rate. Note that these radii correspond to empty spheres present in the ices, while pores can be extended (i.e., non-spherical) volumes. Therefore, our estimates give lower limits of the sizes of the pores. Because the water molecules have time to rearrange with a low deposition rate, larger empty spaces are created which allow the formation of larger pores. We conclude that the pure water ices deposited at two deposition rates present different morphologies as seen experimentally in Section 3.1. The total surface area is larger for numerous small pores than for a few large pores. Furthermore, more bonded molecules—as seen during the lowest deposition rate—provide fewer free O–H dangling modes. This can explain the surface-specific O–H dangling modes observed in the mid-infrared spectra of the pure water ice grown with a  $10 \text{ nm s}^{-1}$  deposition rate. During conditions of low deposition rate, the rearrangement of water molecules implies also more compactness. This is an important criterion when using the EMAs since reference

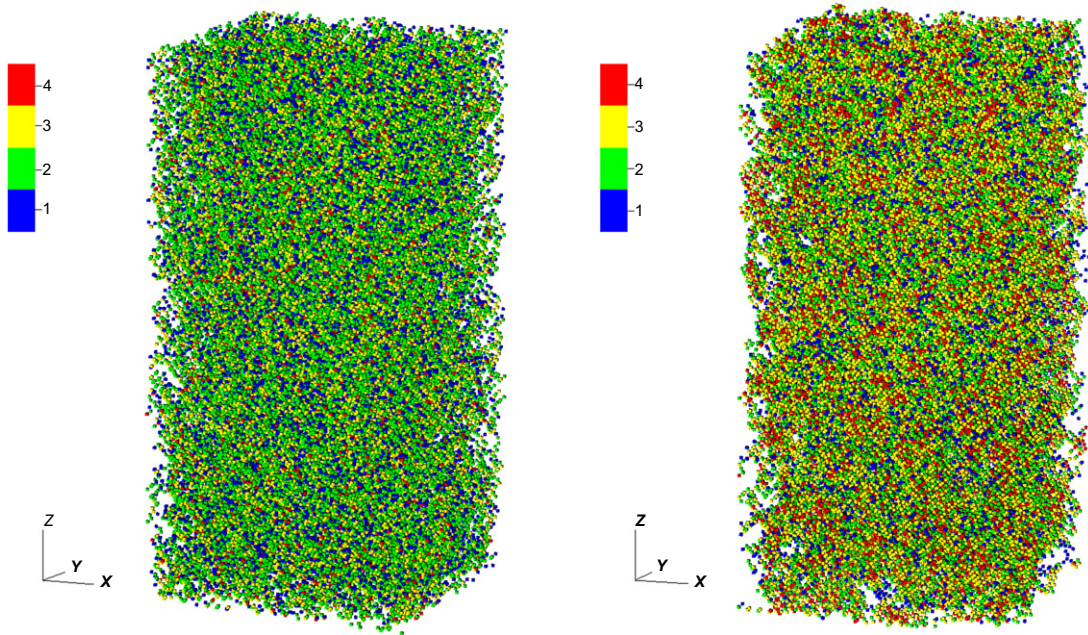


**Figure 9.** Structure of an amorphous solid water ice in a  $100 \times 100 \times 800$  grid, grown at 30 K with a deposition rate of  $10 \text{ nm s}^{-1}$  (*left*) and  $0.2 \text{ nm s}^{-1}$  (*right*). The colors represent the number of neighbors of each molecule.

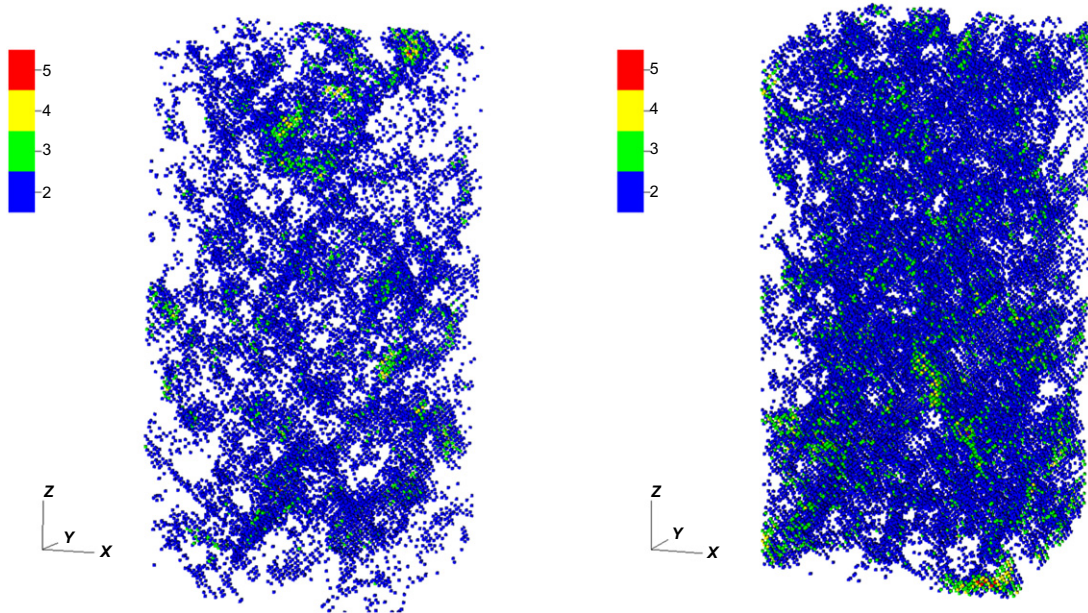


**Figure 10.** Distribution of the pores at 30 K in a  $100 \times 100 \times 800$  grid with a deposition rate of  $10 \text{ nm s}^{-1}$  (*left*) and  $0.2 \text{ nm s}^{-1}$  (*right*). Each dot shows an empty space with a tag  $n$  (color scale) corresponding to the number of empty cells in a radius  $n$  around the cell  $n$ . These numbers are directly related to the size of the pores (e.g., pore 5 has a radius of  $5 \times 2.75 \text{ \AA}$ ). This figure is the negative image of Figure 9.

optical constants of pure and compact species are needed. Although the simulations present less than fully compact water ices, we used the experimental mid-infrared optical constants ( $n_1^{\bar{\nu}} - ik_1^{\bar{\nu}}$ ) coming from the pure ices grown with the lowest deposition rate, thus ensuring the most compact structure.

#### 4. ASTROPHYSICAL IMPLICATIONS

The porosity is a crucial parameter that defines the efficiency of adsorption, diffusion, and reaction, as well as the entrapment

capacities of molecules in interstellar ices. By providing large effective surface areas, pores have important consequences for the chemistry driven by surface processes. The presence of pores, as well as the evolution of the porosity during the different stages of star formation, are key to understanding the molecular complexity seen toward low-mass and high-mass protostars, but also in comets. Porous ices can undergo thermally induced structural collapse, thus affecting the diffusion of the interstellar ice components and therefore the catalytic properties (Bossa et al. 2012; Isokoski et al. 2014;

Cazaux et al. 2015). In this study, we show that low deposition rates allow for the water molecules to reorganize and form more compact ices with larger pores. This implies that on timescales typically found in the ISM, water molecules freezing onto an icy surface have ample time to reorganize. Interstellar ices formed through accretion are therefore supposed to be filled up with large pores. We have also investigated how the porosity affects the optical constants of accreted molecules relevant to astrophysical environments. As a starting point we choose the  $\text{H}_2\text{O}:\text{CH}_4$  system because of the limited physical and chemical interactions between these two species and also for its relevance to astrophysical environments where clathrate hydrates are present, gas–aerosol interactions are dominating, and grain ice mantles are growing. We find that the porosity does not significantly change the optical properties of the composite ices. However, determinations of ice abundances (column densities) from observational data may suffer from a systematic overestimation by taking the band strengths of the pure and compact ice constituents. We observed, for example, a 10% decrease in the band strength of the bulk O–H stretching mode of water for the most porous sample (19% porosity). Therefore, a precise knowledge of the porosity is important to better quantify the overall band strengths.

The present results hold the potential to determine the porosity of inter- and circumstellar ices in a complementary way, by trying to match observational data and optical constants of multi-phase composite ices, using extended EMAs and radiative transfer models. For this purpose we need to build first an exhaustive database of effective mid-infrared optical constants of fictive porous ice materials composed of the basic ingredients of genuine interstellar ices. The EMAs need to be extended to aggregate structures in which more than three different particles characterized by their intrinsic dielectric constants are embedded in an effective medium. Then we can calculate the absorption and scattering opacities of dust grains embedded in the overall set of fictive composite ices. Predictions of the theoretical absorption signature of ices around young stellar objects can be generated by running a radiative transfer code (RADMC-3D) with parameters constrained using previously published observational results (Rocha & Pilling 2015). The EMAs are more accurate when the composite material retains as far as possible the features of the pure constituents, therefore only cold and largely unprocessed objects are promising for precise quantitative studies. A one-to-one comparison between predicted absorption spectra and observational data will provide the optimized volume fractions from the best match. The optimized volume fraction of pores, subsequently, gives an insight into the level of porosity in a specific source. Molar fractions of other ice constituents can be deduced in a second step by taking into account the densities of pure and compact reference ices.

## 5. SUMMARY AND CONCLUSIONS

The results presented here demonstrate that the extended EMAs can be used in the mid-infrared range to evaluate the porosity, to quantify the relative abundances, and to correct the band strengths of the different compounds that compose an inhomogeneous ice material. This work is therefore relevant for

interpreting specific mid-infrared observational data from preferably cold and largely unprocessed ices around young stellar objects. However, an accurate quantitative approach is only possible when the multi-phase composite ice material retains as far as possible the features of the pure and compact constituents. The main conclusions of the present work are:

1. The morphology and porosity of pure water ices depend strongly on the deposition rate, which also affects the mid-infrared absorption spectra. Low deposition rates, which are typical of the interstellar medium, allow water molecules to reorganize and result in the formation of more compact structures containing large pores. This suggests that interstellar ices formed through accretion are expected to contain large pores.
2. The porosity of an ice mixture grown by background deposition depends strongly on the abundance of the premixed gas-phase constituents. In the case of a porous  $\text{H}_2\text{O}:\text{CH}_4$  ice mixture, the porosity measured after deposition generally decreases with increasing  $\text{CH}_4$  concentration. The same conclusion can be drawn with other molecules such as  $\text{CO}_2$ .
3. The intensity/area of the O–H dangling bonds measured from an infrared spectrum cannot be correlated to the level of porosity of the corresponding ice. Instead, the optical constants in the mid-infrared can be analyzed and confronted with theoretical models to retrieve this information.
4. The  $\text{CH}_4$  band strengths embedded in  $\text{H}_2\text{O}$  with astrophysically relevant ratios are significantly different from those obtained from the pure and compact  $\text{CH}_4$  ice. Using these pure ice  $A$ -values in a mixture may lead to considerable errors, especially in the case of high dilution.
5. The presence of  $\text{CH}_4$  has almost no effect on the bulk O–H stretching mode of  $\text{H}_2\text{O}$ . In contrast, the presence of pores in the mixture produces more subtle changes in the corresponding  $A$ -value with an increase of 10% for the most porous ice mixture compared to pure and compact  $\text{H}_2\text{O}$  ice.

Part of this work was supported by NOVA, the Netherlands Research School for Astronomy, and a Vici grant from the Netherlands Organisation for Scientific Research (NWO). J.-B.B. is grateful for support from the Marie Skłodowska Curie actions and the Intra-European Fellowship (FP7-PEOPLE-2011-IEF-299258). S.C. is supported by the Netherlands Organization for Scientific Research (NWO). B.M. and J. O. were supported by the MINECO of Spain under grant FIS2013-48087-C2-1P. S.P. thanks the Brazilian agencies CNPq, CAPES, INCT-A, and FAPESP (JP2009/18304-0; DR2013/07657-5) for financial support. We also thank A. G. G. M. Tielens for stimulating discussions.

## APPENDIX

### A.1. The Extended Maxwell Garnett EMA

The extended model proposed by Luo (1997) treats the porous composite ice asymmetrically: one can visualize the system as a separated-grain structure in which two different

particles ( $A$  and  $B$ ) are dispersed in a continuous host of dielectric medium  $C$ . The particles are assumed to be spheres of a size and a separation distance smaller than the wavelength of the incident light. In the following, the three different components  $A$ ,  $B$ ,  $C$  are characterized by their dielectric constants  $\epsilon_A^\nu$ ,  $\epsilon_B^\nu$ , and  $\epsilon_C^\nu$ , their experimental (intrinsic) mid-infrared optical constants  $(n_A^\nu - ik_A^\nu)$ ,  $(n_B^\nu - ik_B^\nu)$ , and  $(n_C^\nu - ik_C^\nu)$  obtained following the methodology described in Section 2.1.3, and their volume fractions  $f_A$ ,  $f_B$ , and  $f_C$ . We arbitrarily define the spheres of residual atmosphere (pores) as  $A$ , the spheres of pure and compact methane ice as  $B$ , and the pure and compact water ice as the host material  $C$ . In this way, the volume fraction  $f_A$  corresponds to the porosity. Hence for a porous  $\text{H}_2\text{O}:\text{CH}_4$  ice sample of porosity  $f_A$ , the effective dielectric constant  $\epsilon_{\text{eff}}^\nu$  can be determined by solving the following equation for each ice composition ( $0.01 \leq f_{A,B,C} \leq 0.98$ ) and for each wavenumber  $\nu$  in the mid-infrared (Luo 1997):

spheres of residual atmosphere (pores), spheres of pure and compact methane ice, and spheres of pure and compact water ice are embedded in an effective medium, characterized by an effective dielectric constant ( $\epsilon_{\text{eff}}$ ). In the following, we use the same  $A$ ,  $B$ ,  $C$  nomenclature as in the previous section. Hence for a porous  $\text{H}_2\text{O}:\text{CH}_4$  ice sample of porosity  $f_A$ , the effective dielectric constant  $\epsilon_{\text{eff}}^\nu$  can be determined by solving the following equation for each ice composition ( $0.01 \leq f_{A,B,C} \leq 0.98$ ) and for each wavenumber  $\nu$  in the mid-infrared (Luo 1997):

$$f_A \frac{\epsilon_A - \epsilon_{\text{eff}}}{\epsilon_A + 2\epsilon_{\text{eff}}} + f_B \frac{\epsilon_B - \epsilon_{\text{eff}}}{\epsilon_B + 2\epsilon_{\text{eff}}} + f_C \frac{\epsilon_C - \epsilon_{\text{eff}}}{\epsilon_C + 2\epsilon_{\text{eff}}} = 0, \quad (15)$$

with the condition  $f_A + f_B + f_C = 1$ . As previously, we assume that the dielectric constant of the non-absorbing pores equals 1. Water and methane absorb in the mid-infrared, thus

$$\begin{aligned} p_A \left( (\epsilon_C^\nu - \epsilon_{\text{eff}}^\nu)(\epsilon_A^\nu + 2\epsilon_C^\nu) + f_{AB}(2\epsilon_C^\nu + \epsilon_{\text{eff}}^\nu)(\epsilon_A^\nu - \epsilon_C^\nu) \right) / \left( (\epsilon_C^\nu + 2\epsilon_{\text{eff}}^\nu)(\epsilon_A^\nu + 2\epsilon_C^\nu) \right) \\ + f_{AB}(2\epsilon_C^\nu - 2\epsilon_{\text{eff}}^\nu)(\epsilon_A^\nu - \epsilon_C^\nu) + p_B \left( (\epsilon_C^\nu - \epsilon_{\text{eff}}^\nu)(\epsilon_B^\nu + 2\epsilon_C^\nu) + f_{AB}(2\epsilon_C^\nu + \epsilon_{\text{eff}}^\nu)(\epsilon_B^\nu - \epsilon_C^\nu) \right) / \\ \left( (\epsilon_C^\nu + 2\epsilon_{\text{eff}}^\nu)(\epsilon_B^\nu + 2\epsilon_C^\nu) + f_{AB}(2\epsilon_C^\nu - 2\epsilon_{\text{eff}}^\nu)(\epsilon_B^\nu - \epsilon_C^\nu) \right) = 0, \end{aligned} \quad (13)$$

with  $p_A = f_A/(f_A + f_B)$ ,  $p_B = f_B/(f_A + f_B)$ ,  $f_{AB} = f_A + f_B$ , and the condition  $f_A + f_B + f_C = 1$ . The mathematical approach and methodology can be found in more detail in Luo (1997), based on the research of Niklasson et al. (1981). We assume that the dielectric constant of the non-absorbing pores equals 1. Water and methane have absorption bands in the mid-infrared, thus the extinction coefficients  $k_{\text{eff}}^\nu$  must be taken into account and Equation (13) becomes

Equation (15) can be rewritten as

$$\begin{aligned} f_A \frac{1 - (n_{\text{eff}}^\nu - ik_{\text{eff}}^\nu)^2}{1 + 2(n_{\text{eff}}^\nu - ik_{\text{eff}}^\nu)^2} + f_B \frac{(n_B^\nu - ik_B^\nu)^2 - (n_{\text{eff}}^\nu - ik_{\text{eff}}^\nu)^2}{(n_B^\nu - ik_B^\nu)^2 + 2(n_{\text{eff}}^\nu - ik_{\text{eff}}^\nu)^2} \\ + f_C \frac{(n_C^\nu - ik_C^\nu)^2 - (n_{\text{eff}}^\nu - ik_{\text{eff}}^\nu)^2}{(n_C^\nu - ik_C^\nu)^2 + 2(n_{\text{eff}}^\nu - ik_{\text{eff}}^\nu)^2} = 0. \end{aligned} \quad (16)$$

$$\begin{aligned} p_A \left( \left[ (n_C^\nu - ik_C^\nu)^2 - (n_{\text{eff}}^\nu - ik_{\text{eff}}^\nu)^2 \right] \left[ 1 + 2(n_C^\nu - ik_C^\nu)^2 \right] + f_{AB} \left[ 2(n_C^\nu - ik_C^\nu)^2 + (n_{\text{eff}}^\nu - ik_{\text{eff}}^\nu)^2 \right] \right) \\ \times \left[ 1 - (n_C^\nu - ik_C^\nu)^2 \right] / \left( \left[ (n_C^\nu - ik_C^\nu)^2 + 2(n_{\text{eff}}^\nu - ik_{\text{eff}}^\nu)^2 \right] \times \left[ 1 + 2(n_C^\nu - ik_C^\nu)^2 \right] + f_{AB} \left[ 2(n_C^\nu - ik_C^\nu)^2 \right. \right. \\ \left. \left. - 2(n_{\text{eff}}^\nu - ik_{\text{eff}}^\nu)^2 \right] \left[ 1 - (n_C^\nu - ik_C^\nu)^2 \right] \right) + p_B \left( \left[ (n_C^\nu - ik_C^\nu)^2 - (n_{\text{eff}}^\nu - ik_{\text{eff}}^\nu)^2 \right] \left[ (n_B^\nu - ik_B^\nu)^2 \right. \right. \\ \left. \left. + 2(n_C^\nu - ik_C^\nu)^2 \right] + f_{AB} \left[ 2(n_C^\nu - ik_C^\nu)^2 + (n_{\text{eff}}^\nu - ik_{\text{eff}}^\nu)^2 \right] \left[ (n_B^\nu - ik_B^\nu)^2 - (n_C^\nu - ik_C^\nu)^2 \right] \right) / \\ \left( \left[ (n_C^\nu - ik_C^\nu)^2 + 2(n_{\text{eff}}^\nu - ik_{\text{eff}}^\nu)^2 \right] \left[ (n_B^\nu - ik_B^\nu)^2 + 2(n_C^\nu - ik_C^\nu)^2 \right] + f_{AB} \left[ 2(n_C^\nu - ik_C^\nu)^2 \right. \right. \\ \left. \left. - 2(n_{\text{eff}}^\nu - ik_{\text{eff}}^\nu)^2 \right] \left[ (n_B^\nu - ik_B^\nu)^2 - (n_C^\nu - ik_C^\nu)^2 \right] \right) = 0. \end{aligned} \quad (14)$$

## A.2. The Extended Bruggeman EMA

In contrast to the extended Maxwell Garnett EMA, the extended Bruggeman EMA treats the system symmetrically: one can visualize the system as an aggregate structure where

## REFERENCES

- Accolla, M., Congiu, E., Dulieu, F., et al. 2011, *PCCP*, **13**, 8037  
 Ayotte, P., Smith, S. S., Stevenson, K. P., et al. 2001, *JGR*, **106**, 33387  
 Baciocco, G., Calvani, P., & Cunsolo, S. 1987, *JCP*, **87**, 1913  
 Bergin, E. A., Neufeld, D. A., & Melnick, G. J. 1999, *ApJL*, **510**, L145

- Boogert, A. C. A., Gerakines, P. A., & Whittet, D. C. B. 2015, *ARA&A*, **53**, 541
- Boogert, A. C. A., Pontoppidan, K. M., Knez, C., et al. 2008, *ApJ*, **678**, 985
- Bossa, J.-B., Isokoski, K., de Valois, M. S., & Linnartz, H. 2012, *A&A*, **545**, A82
- Bossa, J.-B., Isokoski, K., Paardekooper, D. M., et al. 2014, *A&A*, **561**, A136
- Bossa, J.-B., Paardekooper, D. M., Isokoski, K., & Linnartz, H. 2015, *PCCP*, **17**, 17346
- Bouilloud, M., Fray, N., Bénilan, Y., et al. 2015, *MNRAS*, **451**, 2145
- Brill, R., & Tippe, A. 1967, *AcCr*, **23**, 343
- Brown, D. E., George, S. M., Huang, C., et al. 1996, *JPhCh*, **100**, 4988
- Bruggeman, D. A. G. 1935, *AnP*, **24**, 636
- Brunetto, R., Caniglia, G., Baratta, G. A., & Palumbo, M. E. 2008, *ApJ*, **686**, 1480
- Cazaux, S., Bossa, J.-B., Linnartz, H., & Tielens, A. G. G. M. 2015, *A&A*, **573**, A16
- Cazaux, S., Cobut, V., Marseille, M., Spaans, M., & Caselli, P. 2010, *A&A*, **522**, A74
- Collings, M. P., Dever, J. W., Fraser, H. J., McCoustra, M. R. S., & Williams, D. A. 2003, *ApJ*, **583**, 1058
- Cuppen, H. M., Ioppolo, S., Romanzin, C., & Linnartz, H. 2010, *PCCP*, **12**, 12077
- Dalton, J. B., Cruikshank, D. P., Stephan, K., et al. 2010, *SSRv*, **153**, 113
- Dartois, E., & Deboffle, D. 2008, *A&A*, **490**, L19
- Dartois, E., Ding, J. J., de Barros, A. L. F., et al. 2013, *A&A*, **557**, A97
- Devlin, J. P., Sadlej, J., & Buch, V. 2001, *JPCA*, **105**, 974
- d'Hendecourt, L. B., & Allamandola, L. J. 1986, *A&AS*, **64**, 453
- Dohnálek, Z., Kimmel, G. A., Ayotte, P., Smith, R. S., & Kay, B. D. 2003, *JChPh*, **118**, 364
- Dulieu, F., Amiaud, L., Congiu, E., et al. 2009, *A&A*, **512**, A30
- Dulieu, F., Congiu, E., Noble, J., et al. 2013, *Nature Scientific Reports*, **3**, 1338
- Escribano, R., Timón, V., Gálvez, O., et al. 2014, *PCCP*, **16**, 16694
- Fayolle, E. C., Bertin, M., Romanzin, C., et al. 2011, *ApJL*, **739**, L36
- Fuchs, G. W., Cuppen, H. M., Ioppolo, S., et al. 2009, *A&A*, **505**, 629
- Gálvez, O., Maté, B., Herrero, V. J., & Escribano, R. 2009, *ApJ*, **703**, 2101
- Gibb, E. L., Mumma, M. J., dello Russo, N., Disanti, M. A., & Magee-Sauer, K. 2003, *Icar*, **165**, 391
- Gibb, E. L., Whittet, D. C. B., Boogert, A. C. A., & Tielens, A. G. G. M. 2004, *ApJ*, **151**, 35
- Greenberg, L. T. 1973, in IAU Symp. 52, Interstellar Dust and Related Topics, ed. J. M. Greenberg & H. C. van de Hulst (Dordrecht: Reidel), **3**
- Grundy, W. M., Schmitt, B., & Quirico, E. 2002, *Icar*, **155**, 486
- Hagen, W., Tielens, A. G. G. M., & Greenberg, J. M. 1981, *CP*, **56**, 367
- Herrero, V. J., Gálvez, O., Maté, B., & Escribano, R. 2010, *PCCP*, **12**, 3164
- Hodyss, R., Johnson, P. V., Stern, J. V., Goguen, J. D., & Kanik, I. 2009, *Icar*, **200**, 338
- Hudgins, D. M., Sandford, S. A., Allamandola, L. J., & Tielens, A. G. G. M. 1993, *ApJ*, **86**, 713
- Hudson, R. L., Gerakines, P. A., & Loeffler, M. J. 2015, *PCCP*, **17**, 12545
- Hudson, R. L., Gerakines, P. A., & Moore, M. H. 2014, *Icar*, **243**, 148
- Ioppolo, S., Cuppen, H. M., Romanzin, C., van Dishoeck, E. F., & Linnartz, H. 2008, *ApJ*, **686**, 1474
- Ioppolo, S., Cuppen, H. M., Romanzin, C., van Dishoeck, E. F., & Linnartz, H. 2010, *PCCP*, **12**, 12065
- Isaacs, E. D., Shukla, A., Platzman, P. M., et al. 1999, *PhRvL*, **82**, 600
- Isokoski, K., Bossa, J.-B., Triemstra, T., & Linnartz, H. 2014, *PCCP*, **16**, 3456
- Jayannavar, A. M., & Kumar, N. 1991, *PhRvB*, **44**, 12014
- Keane, J. V., Boogert, A. C. A., Tielens, A. G. G. M., Ehrenfreund, P., & Schutte, W. A. 2001, *A&A*, **375**, L43
- Lagarias, J. C., Reeds, J. A., Wright, M. H., & Wright, P. E. 1998, *SIAM Journal of Optimization*, **9**, 112
- Licandro, J., Grundy, W. M., Pinilla-Alonso, N., & Leisy, P. 2006, *A&A*, **458**, L5
- Linnartz, H., Ioppolo, S., & Fedoseev, G. 2015, *IRPC*, **34**, 205
- Luo, R. 1997, *ApOpt*, **36**, 8153
- Martonchik, J. V., & Orton, G. S. 1994, *ApOpt*, **33**, 8306
- Mastrapa, R. M., Bernstein, M. P., Sandford, S. A., et al. 2008, *Icar*, **197**, 307
- Mastrapa, R. M., Sandford, S. A., Roush, T. L., Cruikshank, D. P., & Ore, C. M. D. 2009, *ApJ*, **701**, 1347
- Maté, B., Rodríguez-Lazcano, Y., & Herrero, V. J. 2012, *PCCP*, **14**, 10595
- Maxwell Garnett, J. C. 1904, *RSPTA*, **203**, 385
- Maxwell Garnett, J. C. 1906, *RSPTA*, **205**, 237
- McKee, C. F. 1989, *ApJ*, **345**, 782
- Miyauchi, N., Hidaka, H., Chigai, T., et al. 2008, *CPL*, **456**, 27
- Mottier, P., & Valette, S. 1981, *ApOpt*, **203**, 1630
- Mukai, T., & Krätschmer, W. 1986, *EM&P*, **36**, 145
- Mukai, T., & Mukai, S. 1984, *AdSpR*, **4**, 207
- Mukai, T., Mukai, S., & Kikuchi, S. 1987, *A&A*, **187**, 650
- Nicorovici, N. A., McKenzie, D. R., & McPhedran, R. C. 1995, *OptCo*, **117**, 151
- Niklasson, G. A., Granqvist, C. G., & Hunderi, O. 1981, *ApOpt*, **20**, 26
- Oba, Y., Miyauchi, N., Hidaka, H., et al. 2009, *ApJ*, **701**, 464
- Öberg, K. I., Boogert, A. C. A., Pontoppidan, K. M., et al. 2008, *ApJ*, **678**, 1032
- Öberg, K. I., Fraser, H. J., Boogert, A. C. A., et al. 2007, *A&A*, **462**, 1187
- Palumbo, M. E. 2006, *A&A*, **453**, 903
- Palumbo, M. E., Baratta, G. A., Leto, G., & Strazzulla, G. 2010, *JMoSt*, **972**, 64
- Perakis, F., & Hamm, P. 2012, *PCCP*, **14**, 6250
- Pilling, S., Andrade, D. P. P., Neto, A. C., Rittner, R., & de Brito, A. N. 2009, *JPCA*, **113**, 11161
- Raut, U., Fama, M., Loeffler, M. J., & Baragiola, R. A. 2008, *ApJ*, **687**, 1070
- Raut, U., Teolis, B. D., Loeffler, M. J., et al. 2007, *JChPh*, **126**, 244511
- Rocha, W. R. M., & Pilling, S. 2014, *AcSpA*, **123**, 436
- Rocha, W. R. M., & Pilling, S. 2015, *ApJ*, **803**, 18
- Romanzin, C., Ioppolo, S., Cuppen, H. M., van Dishoeck, E. F., & Linnartz, H. 2010, *JChPh*, **134**, 084504
- Satorre, M. Á., Domingo, M., Millán, C., et al. 2008, *P&SS*, **56**, 1748
- Stevenson, K. P., Kimmel, G. A., Dohnálek, Z., Smith, S., & Kay, B. D. 1999, *Sci*, **283**, 1505
- van Dishoeck, E. F., Herbst, E., & Neufeld, D. A. 2013, *ChRv*, **113**, 9043
- Wachniewski, A., & McClung, H. B. 1986, *PhRvB*, **33**, 8053
- Watanabe, N., Nagaoka, A., Shiraki, T., & Kouchi, A. 2004, *ApJ*, **616**, 638
- Westley, M. S., Baratta, G. A., & Baragiola, R. A. 1998, *JChPh*, **108**, 3321
- Williams, J. P., & Cieza, L. A. 2011, *ARA&A*, **49**, 67
- Zanchet, A., Rodríguez-Lazcano, Y., Gálvez, O., et al. 2013, *ApJ*, **777**, 26
- Zondlo, M. A., Onasch, T. B., Waeshawsky, M. S., et al. 1997, *JPCB*, **101**, 10887